Acta Crystallographica Section A
Foundations of Crystallography
ISSN 0108-7673

Received 27 April 2011
Accepted 13 September 2011

© 2011 International Union of Crystallography
Printed in Singapore – all rights reserved

Polarization-dependent X-ray six-beam pinhole topographs for a channel-cut silicon crystal

Kouhei Okitsu,[a]* Yoshitaka Yoda,[b] Yasuhiko Imai[b] and Yoshinori Ueji[c]

[a]Nano-Engineering Research Center, Institute of Engineering Innovation, Graduate School of Engineering, The University of Tokyo, 2-11-16 Yayoi, Bunkyo-ku, Tokyo 113-8656, Japan, [b]Japan Synchrotron Radiation Research Institute, SPring-8, 1-1-1 Kouto, Mikazuki-cho, Sayo-gun, Hyogo 679-5198, Japan, and [c]Rigaku Corporation, 3-9-12 Matsubara, Akishima-shi, Tokyo 196-8666, Japan. Correspondence e-mail: okitsu@soyak.t.u-tokyo.ac.jp

It was pointed out in a previous paper [Okitsu *et al.* (2006), *Acta Cryst.* A**62**, 237–244] that an *n*-beam Takagi–Taupin (T–T) equation can be solved for a crystal of arbitrary shape. The procedure to integrate the *n*-beam T–T equation is to let all the Fourier coefficients of the electric susceptibility be zero at positions inside the Borrmann pyramid but outside the crystal. The efficiency of this simple procedure is verified in the present paper by showing qualitative and quantitative agreements between experimentally obtained and computer-simulated X-ray six-beam pinhole topographs for a channel-cut silicon crystal.

1. Introduction

The most widely known X-ray dynamical diffraction theory is the Ewald–Laue (E–L) theory (Ewald, 1917; Laue, 1931) that can deal with an X-ray wavefield in a perfect crystal in which transmitted and only one reflected X-ray beams are strong (the two-beam case). In the late 1960s an X-ray three-beam dynamical theory based on the E–L formulation that can deal with the case in which transmitted and two reflected X-ray beams are strong (the three-beam case) in a perfect crystal was presented by Hildebrandt (1967), by Ewald & Héno (1968) and by Héno & Ewald (1968). Colella (1974) developed a numerical method to solve the *n*-beam E–L theory and experimentally demonstrated obtaining phase triplets of structure factors of a germanium crystal by measuring diffraction profiles of goniometry in the vicinity of three-beam conditions.

On the other hand, the Takagi–Taupin (T–T) equation (Takagi, 1962, 1969; Taupin, 1964) is well known as another X-ray dynamical theory that can deal with a two-beam X-ray wavefield in a distorted crystal. The first extension of the T–T theory to the three-beam case was presented by Thorkildsen (1987) neglecting the polarization effect. A consideration on the three-beam T–T equation when analytically solving it taking into account the polarization effect was given by Larsen & Thorkildsen (1998). However, it was limited to a special case that the authors referred to as 'symmetrical scattering'. An *n*-beam T–T equation ($n \leq 12$), taking into account the polarization effect, and a numerical method to solve it were given for the first time by Okitsu (2003; hereafter denoted O2003) and Okitsu *et al.* (2006; hereafter denoted O *et al.* 2006). They have been verified from qualitative (Okitsu *et al.*, 2003) and quantitative (O *et al.* 2006) agreements between experimentally obtained and computer-simulated six-beam pinhole topographs for a parallel-plate silicon crystal.

In O 2003 and O *et al.* 2006 it was also pointed out that the *n*-beam T–T equation can be numerically solved for a crystal with an arbitrary shape. This is an important advantage compared with the *n*-beam E–L theory whose solution cannot directly be obtained for a crystal with a complex shape. In the present paper it is clarified that the *n*-beam T–T equation can be numerically solved for a crystal with an arbitrary shape by showing qualitative and quantitative agreements between experimentally obtained and computer-simulated polarization-dependent six-beam pinhole topographs for a channel-cut silicon crystal.

2. Computer simulation

The procedure to obtain computer-simulated pinhole topograph images shown in §4 of the present paper is fundamentally the same as that described in §3 of O 2003 and §3 of O *et al.* 2006.

Fig. 1 shows the dimensions of the channel-cut silicon crystal and the position on which X-rays transmitted through a pinhole were incident such that a six-beam condition was satisfied. The calculation was performed layer by layer, with layer thickness $T_{\rm h}/3600$, scanning the whole region inside the 'virtual Borrmann hexagonal pyramid' with $T_{\rm h}$ being 18.2 mm. Here, $T_{\rm h}$ is the thickness of the crystal shown in Fig. 1. The values of $\chi_{h_i-h_j}$ in equation (8) of O *et al.* 2006 were assumed to be as summarized in Table 1 for a photon energy of 18.475 keV when the middle point between $R_k^{(0)}$ and $R^{(1)}$ ($k \in \{0, 1, 2, 3, 4, 5\}$) in Fig. 2(*a*) of O *et al.* 2006 was in the crystal. However, all values of $\chi_{h_i-h_j}$ were assumed to be zero when the middle point between $R_k^{(0)}$ and $R^{(1)}$ was in the

Table 1
Parameters of X-ray reflection indices of the silicon crystal for a photon energy of 18.475 keV (a wavelength of 0.6711 Å) calculated by using *XINPRO* of *XOP* (version 2.11) (del Rio & Dejus, 1998).

θ_B is the Bragg reflection angle; $|F_\mathbf{h}|$ is the absolute value of the crystal structure factor; $|\chi_{\mathbf{h}r}|$ and $|\chi_{\mathbf{h}i}|$ are absolute values of the real and imaginary parts of $\chi_\mathbf{h}$. Here, $\chi_\mathbf{h}$ is the **h**th-order Fourier coefficient of electric susceptibility of the silicon crystal. $\Lambda_L^{(\sigma)}$ and $\Lambda_L^{(\pi)}$ are the Pendellösung distances for σ and π polarization in the two-beam case defined by Authier (2005).

h	$2\theta_B$ (°)	$\lvert F_\mathbf{h}\rvert$	$\lvert\chi_{\mathbf{h}r}\rvert$ $\times 10^6$	$\lvert\chi_{\mathbf{h}i}\rvert$ $\times 10^7$	$\Lambda_L^{(\sigma)}$ (μm)	$\Lambda_L^{(\pi)}$ (μm)
0 0 0	0.0000	114.0007	2.8424	0.1267	23.61	23.61
4 4 0	40.9143	43.5906	1.0992	0.1116	57.20	75.70
4 8 4	74.5101	16.8270	0.4242	0.0866	125.92	471.50
0 8 8	88.6959	12.1786	0.3070	0.0763	156.32	6868.7
$\bar{4}$ 4 8	74.5101	16.8270	0.4242	0.0866	125.92	471.50
$\bar{4}$ 0 4	40.9143	43.5906	1.0992	0.1116	57.20	75.70

atmospheric region. Since equation (8) of O *et al.* 2006 contains the term χ_o explicitly, this procedure is effective in solving the *n*-beam T–T equation for a crystal with an arbitrary shape.

Each calculation under the assumption of incident horizontal-linearly (LH) and vertical-linearly (LV) polarized X-rays took about 2 h using 32 CPUs (128 cores) of an SGI Altix ICE 8400EX supercomputer system. This short computing time, compared with that in the case of O *et al.* 2006, is mainly due to the parallelization of program code and the recent rapid development of supercomputers. A set of X-ray amplitudes simulated under an assumption of incident X-rays with an arbitrary state of polarization was obtained by using the procedure described in the last paragraph in §3 of O *et al.* 2006.

The polarization states of incident X-rays for comparison with the experimental results were assumed as summarized in Table 2 in order to obtain the computer-simulated topographs. The procedure for obtaining the values of χ_{MA} and R used for the simulations is described in a separate paper (Okitsu, 2011).

The tones of all computer-simulated images with a pixel size of 50×50 μm were tuned using an identical tone curve using Adobe Photoshop CS4.

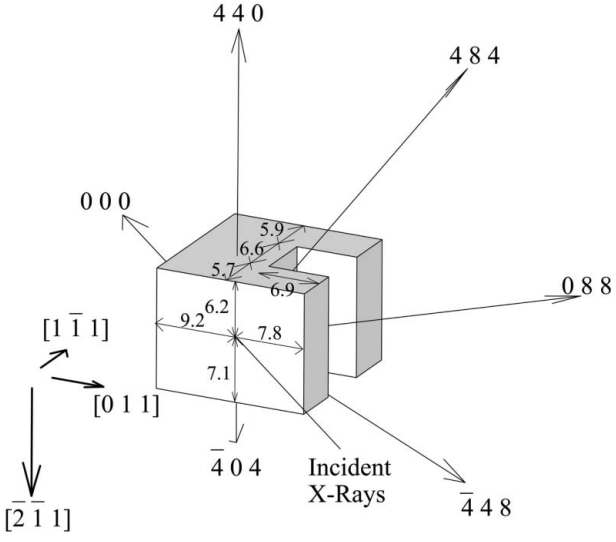

Figure 1
The shape and dimensions (mm) of the silicon crystal used in the experiment and assumed in the computer simulation. The X-ray beam (18.475 keV) with dimensions of 100×100 μm was incident at the position on the crystal surface shown in the figure. Only at this position was a non-zero value of the amplitude of the incident X-rays given for the boundary condition numerically to solve the *n*-beam T–T equation ($n = 6$).

3. Experimental

Fig. 2 shows the experimental arrangement at BL09XU of SPring-8 with which the experimental six-beam pinhole topographs were obtained. The first-order undulator X-ray beam was monochromated to 18.475 keV (a wavelength of 0.6711 Å) with a water-cooled silicon monochromator system giving a twice-bounced 1 1 1 reflection and transmitted through a slit system of size 100×100 μm. Then the polarization state of the X-rays was controlled using a four-quadrant phase-retarder system (Okitsu *et al.*, 2002) that can be rotated around the transmitted beam axis (see Fig. 3 in O *et al.* 2006).

The arrangement of the diamond phase-retarder crystals was identical with that described using Fig. 3 in §4.1 of O *et al.* 2006. However, the values of χ_{PR} and angular deviations of the diamond crystals from the Bragg condition $\Delta\theta_{PRn}$ ($n \in \{1, 2, 3, 4\}$) were different from those used in the experiment of O *et al.* 2006. These values in the present work are summarized in Table 2. When $\Delta\theta_{PRn}$ is positive, the *n*-numbered-quadrant phase retarder is angularly deviated from the Bragg angle to the high-angle side by $\Delta\theta_{PRn}$. When $\chi_{PR} = 0$, the planes of incidence of the first-, second-, third- and fourth-quadrant phase retarders are inclined by 45°, 135°, 225° and 315°, respectively. The thicknesses of these [1 0 0]-oriented diamond crystals were 1.545, 2.198, 1.565 and 2.633 mm, respectively. χ_{PR} is positive when the χ_{PR} axis is rotated counterclockwise as viewed from the downstream direction. $\Delta\varphi_{total}$, χ_{MA} and R are the total phase shift given by the phase retarder system, the inclined angle of the major axis, and the ellipticity of the practically generated polarization state of the X-rays by the phase retarder system that are calculated based on a procedure described in a separate paper (Okitsu, 2011).

Then, the X-rays were incident on the position on the sample crystal shown in Fig. 1. The sample was a floating-zone silicon channel-cut crystal with a high resistivity (>2000 Ω cm) whose surfaces were chemically etched. The goniometer on which the sample was mounted had four (ω, φ, θ and χ) axes. The ω, φ and θ axes were approximately parallel to the directions of [1 $\bar{1}$ 1], [0 1 1] and [$\bar{2}$ $\bar{1}$ 1] of the sample crystal, respectively. The χ axis was approximately parallel to the transmitted X-ray beam axis. The χ and ω axes were adjusted such that the [2 1 $\bar{1}$] direction of the sample crystal was vertical.

The 0 0 0-forward-diffracted (hereafter referred to as FD) and 4 4 0- and 4 8 4-transmitted-reflected (hereafter referred

Table 2
χ_{PR} and $\Delta\theta_{PRn}$ ($n \in \{1, 2, 3, 4\}$) are summarized for generating horizontal linear (LH), approximately vertical linear (LV), approximately −45°-inclined linear (L-45°) and approximately left-screwed-circular (CL) polarizations with which the experimental pinhole topographs were recorded.

Intended polarization	χ_{PR} (°)	$\Delta\theta_{PR1}$ (arcsec)	$\Delta\theta_{PR2}$ (arcsec)	$\Delta\theta_{PR3}$ (arcsec)	$\Delta\theta_{PR4}$ (arcsec)	$\Delta\varphi_{total}/\pi$	χ_{MA} (°)	R
LH	0	26.00	36.96	26.32	44.28	0.000	0.000	0.000
LV	0	14.80	−17.64	14.88	−19.32	0.9027	90.000	0.228
L-45°	+22.5	14.80	−17.64	14.88	−19.32	0.9027	−43.507	0.157
CL	0	27.52	−32.80	27.68	−35.92	0.4671	0.000	0.836

to as TR) X-ray intensities were simultaneously monitored using PIN photodiodes PIN_{000}, PIN_{440} and PIN_{484}. The angular position for satisfying the six-beam condition was searched for by rotating the θ and φ axes such that the X-ray intensities detected by PIN_{000}, PIN_{440} and PIN_{484} had maximum values simultaneously. Then, an imaging plate (IP) was placed 24 mm behind the exit surface of the crystal to record 0 0 0-FD and 4 4 0-, 4 8 4-, 0 8 8-, $\bar{4}$ 4 8- and $\bar{4}$ 0 4-TR six-beam pinhole topograph images simultaneously. The surface of the IP was perpendicular to the [1 $\bar{1}$ 1] direction of the sample crystal. The exposure time was 900 s for all the experimental topograph images shown in Figs. 3–5. The images were read by a Fuji BAS-2500 IP reader with 50 × 50 μm pixel size. All experimental and computer-simulated pinhole topographs in the present paper are negative images.

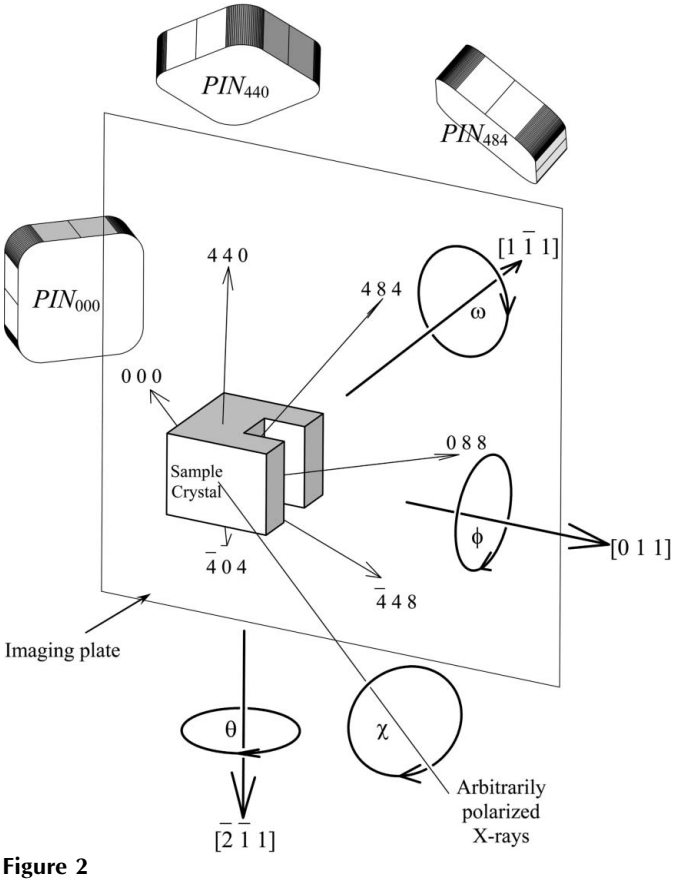

Figure 2
Experimental arrangement used to record the pinhole topographs with the channel-cut floating-zone silicon crystal on the imaging plate 24 mm behind the sample.

4. Results and discussion

Fig. 3 shows (*a*) experimentally obtained and (*b*) computer-simulated six-beam pinhole topographs using incident LH-polarized X-rays. An excellent qualitative agreement between Figs. 3(*a*) and 3(*b*) can be found. This qualitatively validates the computer algorithm described in §2 of the present paper to solve the *n*-beam T–T equation (4) of O *et al.* 2006 for a perfect crystal with a complex shape. Figs. 4 and 5 are enlarged pinhole topograph images, $[E(x)]$ experimentally obtained and $[S(x)]$ computer-simulated for 0 0 0-FD and 4 4 0-TR X-rays where $x \in \{a, b, c, d\}$. Figs. 4 $[X(a)]$ and 5 $[X(a)]$ ($X \in \{E, S\}$) are enlargements of Figs. 3(*a*) and 3(*b*). $[X(b)]$, $[X(c)]$ and $[X(d)]$ of Figs. 4 and 5 were obtained using incident X-rays polarized approximately vertical-linearly (LV), approximately −45°-inclined-linearly (L-45°) and approximately left-screwed-circularly (CL), respectively, that were generated with the phase-retarder system or assumed in the simulation. Precise discussions about the polarization states are given in a separate paper (Okitsu, 2011). Excellent qualitative agreements in detail between the experimentally obtained and computer-simulated images can be found. Furthermore, $[X(a)]$, $[X(b)]$, $[X(c)]$ and $[X(d)]$ of Figs. 4 and 5 are evidently different from one another depending on the difference in polarization state of the incident X-rays. In particular, conspicuous differences are found between $[X(a)]$ and $[X(b)]$.

Figs. 6(*a*) and 7(*a*) are enlargements of parts $[S(a)]$ and $[S(b)]$ of Fig. 5. The lower curves in (α), (β), (γ) and (δ) of Figs. 6 and 7 are cross-section X-ray intensity profiles at the black horizontal lines α, β, γ and δ in Figs. 6(*a*) and 7(*a*). The upper curves are the corresponding profiles extracted from parts $[E(a)]$ and $[E(b)]$ of Fig. 5. A quantitative agreement can be found between computer-simulated and experimentally obtained intensity profiles in (α), (β), (γ) and (δ) of Figs. 6 and 7. Characteristic patterns are observed in these figures, *i.e.* two fine fringe regions [FFR(1) and FFR(2)], a very bright region (VBR), and a square region (SqR) surrounded by boundary lines (BL). A large circle (COut) found in Fig. 6(*a*) is not found in Fig. 7(*a*). However, a small circle (CIn) found in Fig. 7(*a*) is not found in Fig. 6(*a*). A concentric circular region (CCR) found inside COut in Fig. 6(*a*) is very faint in Fig. 7(*a*). Four radial patterns like spikes, Sp(1), Sp(2), Sp(3) and Sp(4), are extended from CP in Fig. 6(*a*). On the other hand, only Sp(1) is found in Fig. 7(*a*). Faint patterns like clouds, Cl(1), Cl(2) and Cl(3), floating on the background region (BGR) are not noise but true signals since they are also found in $[E(x)]$ and $[S(x)]$ ($x \in \{a, b, c, d\}$) of Fig. 5. Differences are also found between the experimentally obtained and computer-simulated topographs, *i.e.* the diameters of CIn and COut, which are considered to be caused by slight differences in $\chi_{h_i - h_j}$ between practical values and values assumed in the simulation.

Figs. 8(*a*) and 8(*b*) are computer-simulated pinhole topographs for a parallel-plate crystal with the same thickness (18.2 mm) under the assumptions of incident (*a*) LH- and (*b*)

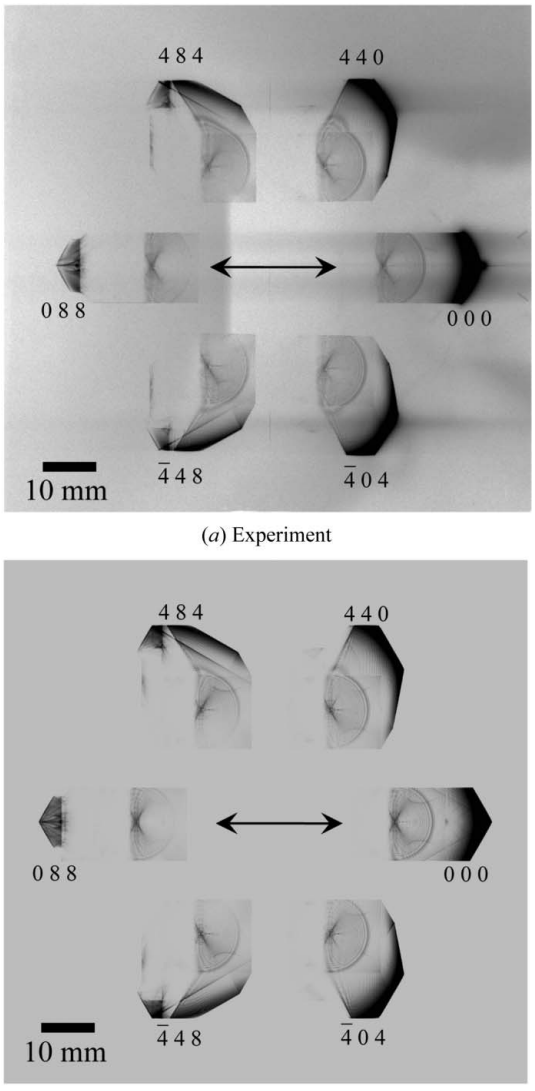

Figure 3
(*a*) Experimentally obtained and (*b*) computer-simulated pinhole topograph images using incident horizontal-linearly (LH) polarized X-rays.

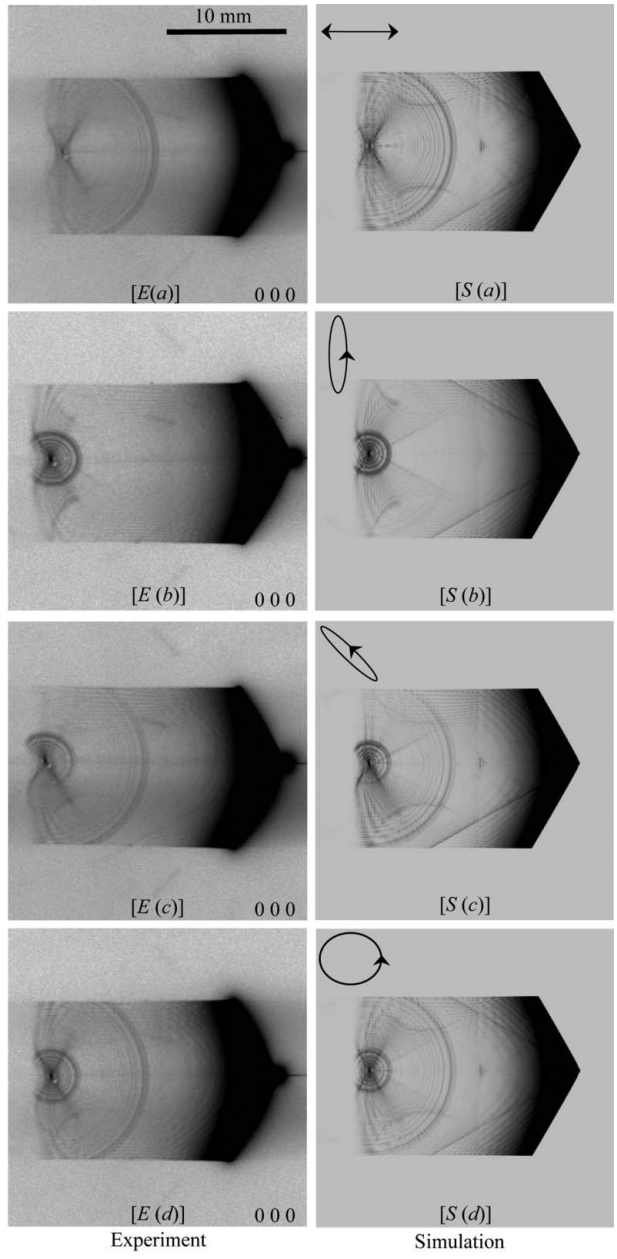

Figure 4
Experimentally obtained and computer-simulated pinhole topograph images of 0 0 0-forward-diffracted (FD) X-rays with the channel-cut silicon crystal. The incident X-rays for (*a*), (*b*), (*c*) and (*d*) are polarized LH, approximately vertical-linearly (LV), approximately −45°-inclined-linearly (L-45°) and approximately left-screwed-circularly (CL) (see Table 2 for details), respectively.

approximately LV-polarized X-rays. COut and CIn are also found in Figs. 8(*a*) and 8(*b*), which reveal the existence of cone-shaped energy-flow paths depending on the polarization state of the incident X-rays.

All computer-simulated pinhole topographs shown in O *et al.* 2006 and the present paper were obtained not taking into account the finite pinhole sizes, 25 × 25 μm in O *et al.* 2006 and 100 × 100 μm in the present paper. The present authors considered that convolution of computer-simulated X-ray intensities with the apertures of pinholes was not necessary because the size of the pinhole was sufficiently small compared with the image sizes of topographs and of the same order of magnitude as the pixel size (50 × 50 μm) of all experimentally obtained and computer-simulated pinhole topographs.

Several experimental and theoretical works on six-beam cases can be found over the last four decades (Afanas'ev & Kohn, 1977; Besirganyan *et al.*, 1984; Kohn & Toneyan, 1986; Kazimirov *et al.*, 1993). The theoretical parts of these works were all based on the E–L theory. Kohn & Toneyan (1986) discussed six-beam diffraction taking into account the source–crystal–film distance. In the case of the present paper, however, the distance between the crystal and the imaging plate (24 mm) was considered to be negligibly small. Further, the condition of spherical-wave incidence was probably satisfied in spite of the source–crystal distance over 10 m.

The E–L theory in which the dispersion surfaces can be defined is very effective for intuitive and qualitative under-

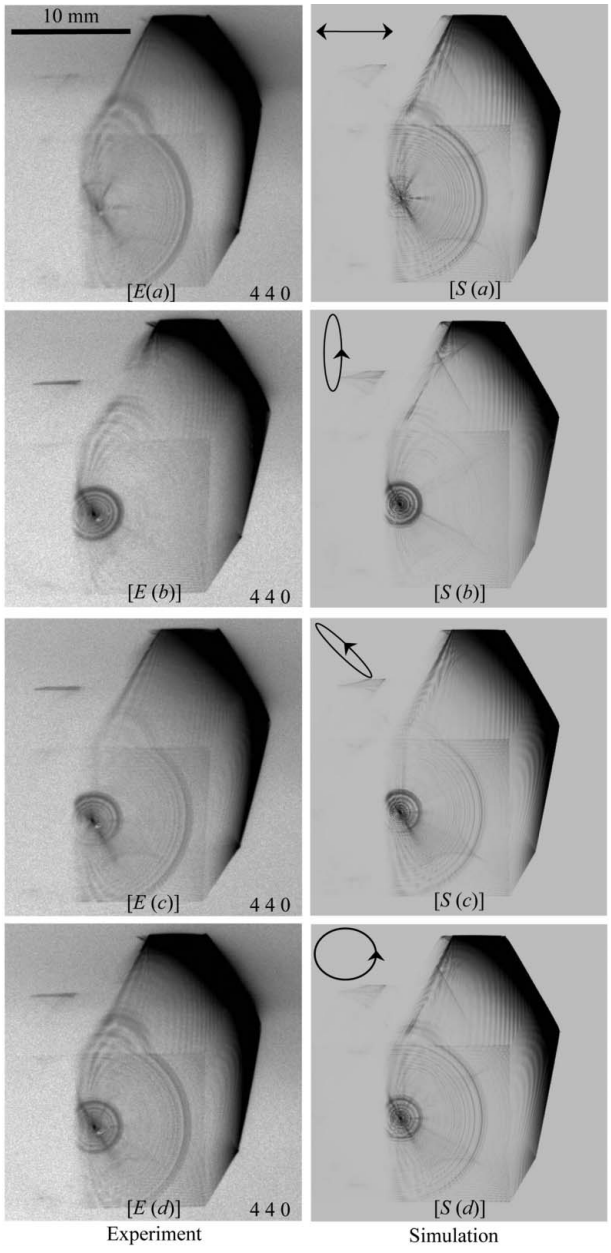

Figure 5
Experimentally obtained and computer-simulated pinhole topograph images of 4 4 0-transmitted-reflected (TR) X-rays with the channel-cut silicon crystal. The polarization states of incident X-rays for (*a*), (*b*), (*c*) and (*d*) are LH, approximately LV, approximately L-45° and approximately CL (see Table 2 for details), respectively.

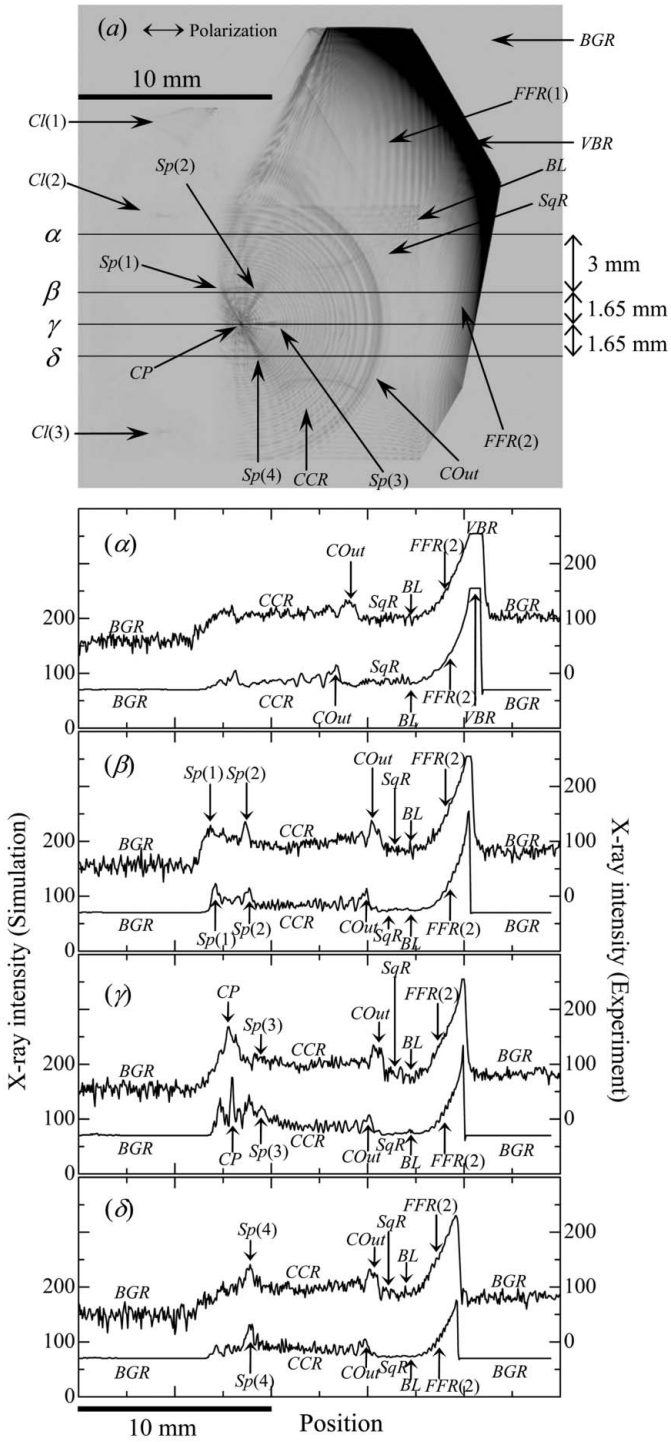

Figure 6
(*a*) Enlargement of Fig. 5 [*S*(*a*)] using incident LH-polarized X-rays. The lower curves of (α), (β), (γ) and (δ) are cross-section X-ray intensity profiles at the horizontal black lines α, β, γ and δ, respectively, in (*a*). The upper curves are experimental cross-section profiles corresponding to the computer-simulated ones. These upper curves were extracted from Fig. 5 [*E*(*a*)].

standing of the behavior of X-rays especially in two-beam cases. Pendellösung distances for σ and π polarizations in the two-beam cases are summarized in the last two columns of Table 1. Spacings of circular and linear fine fringes observed in Figs. 6 and 7 are approximately equal to the Pendellösung distances for the 4 4 0 reflection. The Pendellösung distance can be clearly understood from the gap between dispersion surfaces in two-beam cases. In the case of *n*-beam diffraction, however, the behavior of X-rays is too complex intuitively to understand, mainly owing to the polarization coupling effect.

The suppression of absorption by the Borrmann effect in the two-beam case is observed at the central part of the bottom of the Borrmann fan. However, Figs. 3, 4 and 8 reveal that the enhancement of the Borrmann effect (Borrmann & Hartwig, 1965) took place not at the central region but at a peripheral region of the bottom of the hexagonal Borrmann pyramid. If the undulator synchrotron X-rays, not mono-

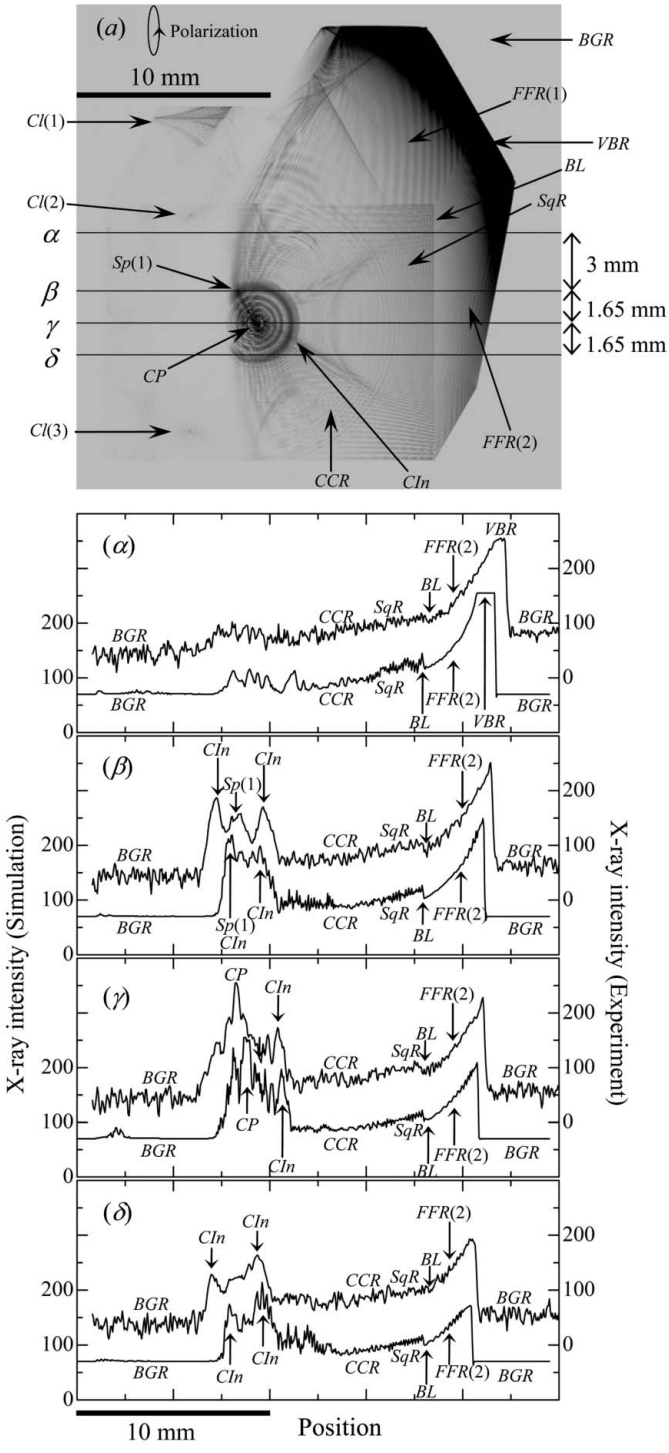

Figure 7
(*a*) Enlargement of Fig. 5 [*S*(*b*)] using incident approximately LV-polarized X-rays (see Table 2 for details). The lower curves of (α), (β), (γ) and (δ) are cross-section X-ray intensity profiles at the horizontal black lines α, β, γ and δ, respectively, in (*a*). The upper curves are experimental cross-section profiles corresponding to the computer-simulated ones. These upper curves were extracted from Fig. 5 [*E*(*b*)].

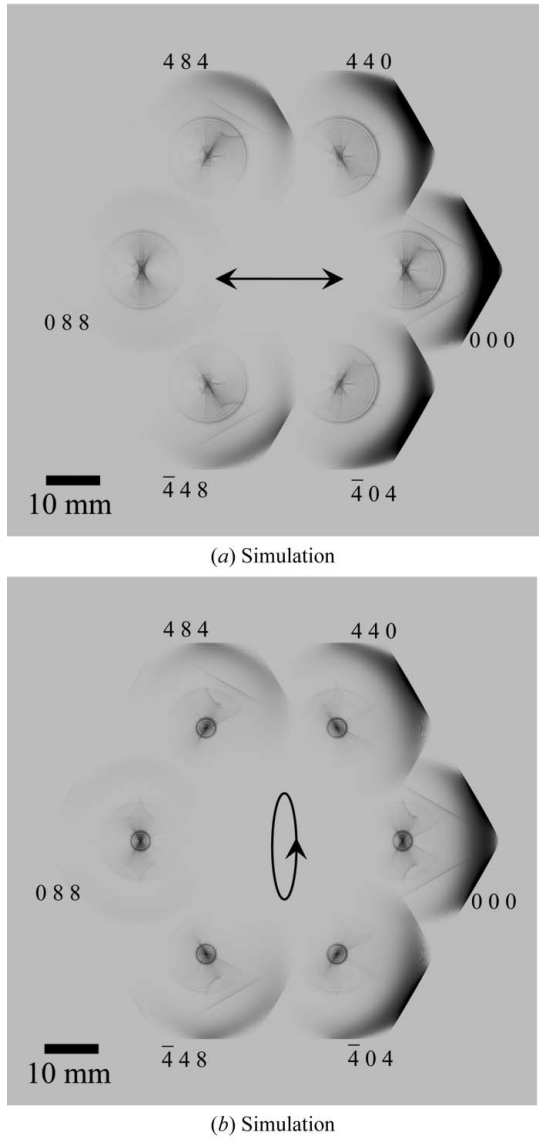

Figure 8
Computer-simulated pinhole topographs for a parallel-plate silicon crystal with a thickness of 18.2 mm for incidence of X-rays (*a*) LH-polarized and (*b*) approximately LV-polarized. The other conditions assumed are identical to those for the channel-cut crystal.

chromated and just transmitted through a pinhole, were incident on a thick silicon crystal as used in the present experiment, the crystal might work as a transmission-type monochromator utilizing the super-Borrmann effect. The polarization state of the pinhole beam extracted from the bright region of Fig. 5 [*E*(*a*)] would be controlled to be identical to that at the corresponding position of Fig. 5 [*S*(*a*)].

The T–T theory is frequently regarded as a special theory that can deal with lattice distortion and directly can deal with spherical-wave X-ray incidence. The T–T and E–L theories should be used as appropriate for the purpose, based on the recognition that these theories are equivalent. The T–T equation describes the X-ray wavefield in real space whereas the E–L theory describes that in reciprocal space. It can be considered that, for this reason, the T–T equation acquired the significant advantage of dealing with an arbitrarily shaped crystal, on which the present paper reports for the six-beam case, in addition to dealing with an arbitrarily deformed crystal, which is widely recognized.

5. Conclusion

Excellent qualitative and quantitative agreements were found between experimentally obtained and computer-simulated pinhole topographs for a channel-cut silicon crystal. This validated the computer algorithm for solving the X-ray n-beam dynamical theory (Okitsu, 2003; Okitsu *et al.*, 2003, 2006) based on the T–T formulation (Takagi, 1962, 1969; Taupin, 1964) for a crystal with a complex shape. The characteristic feature of this algorithm is to deal with the Fourier coefficients of electric susceptibility $\chi_{h_i-h_j}$ $(i, j \in \{0, 1, 2, \cdots, n-1\})$ in equation (8) of O *et al.* 2006 as functions of position. The X-ray wavefield in a crystal of arbitrary shape can be solved by distinguishing the atmospheric position where χ_o and $\chi_{h_i-h_j}$ $(i \neq j)$ are all zero from the position in the crystal where χ_o and $\chi_{h_i-h_j}(i \neq j)$ have finite values.

The conventional approaches to solving the phase problem using the n-beam method were all based on the n-beam dynamical theory described by the E–L formulation. However, the advantage of the n-beam T–T dynamical theory that is applicable to a crystal of arbitrary shape over the E–L-type n-beam theory has been shown in the present work.

The theoretical work and coding of computer programs of the present work were performed at the High-Power X-ray Laboratory, Nano-Engineering Research Center, Institute of Engineering Innovation, Graduate School of Engineering, The University of Tokyo, Japan. The computer-simulated pinhole topographs were obtained using the facilities of the Supercomputer Center, Institute for Solid State Physics, The University of Tokyo, Japan. Preliminary experiments were performed at BL15C and ARNE3A of the Photon Factory of KEK under the approval of the Photon Factory Program Advisory Committee (Proposal No. 2003G202, 2003G203). The experimental pinhole topographs shown in the present paper were obtained at BL09XU of SPring-8 under the approval of the Japan Synchrotron Radiation Research Institute (JASRI) (Proposal No. 2004A0330-ND3c-np). The present work is one of the activities of the Active Nano-Characterization and Technology Project financially supported by the Special Coordination Fund of the Ministry of Education, Culture, Sports, Science and Technology of the Japanese government. The authors are indebted to Professor Emeritus S. Kikuta of The University of Tokyo for his encouragement of the present study and are also indebted to Dr T. Oguchi of SPring-8 Service Company for his technical assistance with the experiment.

References

Afanas'ev, A. M. & Kohn, V. G. (1977). *Acta Cryst.* A**33**, 178–184.
Authier, A. (2005). *Dynamical Theory of X-ray Diffraction*, reprinted with revisions 2004, 2005. Oxford University Press.
Besirganyan, P. A., Gabrielyan, R. T. & Kohn, V. G. (1984). *Phys. Status Solidi A*, **85**, 349–358.
Borrmann, G. & Hartwig, W. (1965). *Z. Kristallogr.* **121**, 401–409.
Colella, R. (1974). *Acta Cryst.* A**30**, 413–423.
Ewald, P. P. (1917). *Ann. Phys.* **54**, 519–597.
Ewald, P. P. & Héno, Y. (1968). *Acta Cryst.* A**24**, 5–15.
Héno, Y. & Ewald, P. P. (1968). *Acta Cryst.* A**24**, 16–42.
Hildebrandt, G. (1967). *Phys. Status Solidi*, **24**, 245–261.
Kazimirov, A. Y., Kovalchuk, M. V., Kohn, V. G., Ishikawa, T., Kikuta, S. & Hirano, K. (1993). *Euro. Lett.* **24**, 211–216.
Kohn, V. G. & Toneyan, A. H. (1986). *Acta Cryst.* A**42**, 441–449.
Larsen, H. B. & Thorkildsen, G. (1998). *Acta Cryst.* A**54**, 129–136.
Laue, M. V. (1931). *Ergeb. Exakten Naturwiss.* **10**, 133–158.
Okitsu, K. (2003). *Acta Cryst.* A**59**, 235–244.
Okitsu, K. (2011). *Acta Cryst.* A**67**, 557–558.
Okitsu, K., Imai, Y., Ueji, Y. & Yoda, Y. (2003). *Acta Cryst.* A**59**, 311–316.
Okitsu, K., Ueji, Y., Sato, K. & Amemiya, Y. (2002). *Acta Cryst.* A**58**, 146–154.
Okitsu, K., Yoda, Y., Imai, Y., Ueji, Y., Urano, Y. & Zhang, X. (2006). *Acta Cryst.* A**62**, 237–247.
Rio, M. S. del & Dejus, R. J. (1998). *Proc. SPIE*, **3448**, 340–345.
Takagi, S. (1962). *Acta Cryst.* **15**, 1311–1312.
Takagi, S. (1969). *J. Phys. Soc. Jpn*, **26**, 1239–1253.
Taupin, D. (1964). *Bull. Soc. Fr. Minéral. Cristallogr.* **87**, 469–511.
Thorkildsen, G. (1987). *Acta Cryst.* A**43**, 361–369.